

Comparison of synthetic maps from truncated jet-formation models with YSO jet observations

M. Stute^{1,2}, J. Gracia^{3,4,5}, K. Tsinganos², and N. Vlahakis²

¹ Dipartimento di Fisica Generale "A. Avogadro", Università degli Studi di Torino, via Pietro Giuria 1, 10125 Torino, Italy
e-mail: matthias.stute@ph.unito.it

² IASA and Section of Astrophysics, Astronomy and Mechanics, Department of Physics, University of Athens, Panepistimiopolis, 157 84 Zografos, Athens, Greece

³ High Performance Computing Center Stuttgart (HLRS), Universität Stuttgart, 70550 Stuttgart, Germany

⁴ Max-Planck-Institut für Kernphysik, Postfach 10 39 80, 69029 Heidelberg, Germany

⁵ School of Cosmic Physics, Dublin Institute of Advanced Studies, 31 Fitzwilliam Place, Dublin 2, Ireland

Received 21 October 2008 / Accepted 16 April 2010

ABSTRACT

Context. Significant progress has been made in the last years in the understanding of the jet formation mechanism through a combination of numerical simulations and analytical MHD models for outflows characterized by the symmetry of self-similarity. Analytical radially self-similar models successfully describe disk-winds, but need several improvements. In a previous article we introduced models of truncated jets from disks, i.e. evolved in time numerical simulations based on a radially self-similar MHD solution, but including the effects of a finite radius of the jet-emitting disk and thus the outflow.

Aims. These models need now to be compared with available observational data. A direct comparison of the results of combined analytical theoretical models and numerical simulations with observations has not been performed as yet. This is our main goal.

Methods. In order to compare our models with observed jet widths inferred from recent optical images taken with the Hubble Space Telescope (HST) and ground-based adaptive optics (AO) observations, we use a new set of tools to create emission maps in different forbidden lines, from which we determine the jet width as the full-width half-maximum of the emission.

Results. It is shown that the untruncated analytical disk outflow solution considered here cannot fit the small jet widths inferred by observations of several jets. Furthermore, various truncated disk-wind models are examined, whose extracted jet widths range from higher to lower values compared to the observations. Thus, we can fit the observed range of jet widths by tuning our models.

Conclusions. We conclude that truncation is necessary to reproduce the observed jet widths and our simulations limit the possible range of truncation radii. We infer that the truncation radius, which is the radius on the disk mid-plane where the jet-emitting disk switches to a standard disk, must be between around 0.1 up to about 1 AU in the observed sample for the considered disk-wind solution. One disk-wind simulation with an *inner* truncation radius at about 0.11 AU also shows potential for reproducing the observations, but a parameter study is needed.

Key words. magnetohydrodynamics – methods: numerical – ISM: jets and outflows – stars: pre-main sequence

1. Introduction

Astrophysical jets and disks (Livio 2009) seem to be inter-related, notably in young stellar objects (YSOs), where jet signatures are well correlated with the infrared excess and accretion rate of the circumstellar disk (Cabrit et al. 1990; Hartigan et al. 2004). Disks provide the plasma which is outflowing in the jets, while jets in turn provide the disk with the needed angular momentum removal so that accretion onto the protostellar object takes place (Hartmann 2009). On the theoretical front, the most widely accepted description of this accretion-ejection phenomenon (Ferreira 2007) is based on the interaction of a large scale magnetic field with an accretion disk around the central object. Then, plasma is channeled and magneto-centrifugally accelerated along the open magnetic field lines threading the accretion disk, as first described in Blandford & Payne (1982). Several works have extended this study either by semi-analytic models using radially self-similar solutions of the full magnetohydrodynamics (MHD) equations with the disk treated as a boundary condition (Vlahakis & Tsinganos 1998), by self-consistently treating the disk-jet system semi-analytically (e.g. Ferreira 1997;

Casse & Ferreira 2000a), or, by self-consistently treating numerically the disk-jet system (e.g. Zanni et al. 2007; Tzeferacos et al. 2009).

The original Blandford & Payne (1982) model, however, has serious limitations for a needed meaningful comparison of its predictions with observations. First, singularities exist at the jet axis, the outflow is not asymptotically super-fast, and most importantly, an intrinsic scale in the disk is lacking with the result that the jet formally extends to radial infinity, to mention just a few. First, the singularity at the axis can be easily taken care of by numerical simulations extending the analytical solutions close to this symmetry axis (Gracia et al. 2006, GVT06 hereafter). Next, the outflow speed at large distances may be tuned to cross the corresponding limiting characteristic, with the result that the terminal wind solution is causally disconnected from the disk and hence perturbations downstream of the super-fast transition (as modified by self-similarity) cannot affect the whole structure of the steady disk-wind outflow (Vlahakis et al. 2000, V00 hereafter), a state which has also been shown to be structurally stable (Matsakos et al. 2008, M08 hereafter). The next step of introducing a scale in the disk has been done in a

Table 1. List of numerical science models.

Name	Domain [$R_0 \times R_0$]	Resolution	Description	R_{trunc} [R_0]
model SC1a	$[0, 50] \times [6, 100]$	200×400	$\alpha_{\text{trunc}} = 0.4$, external analytical solution $\lambda_1 = 10^3, \lambda_2 = 10^{-3}$	5.375
model SC1b	$[0, 50] \times [6, 100]$	200×400	$\alpha_{\text{trunc}} = 0.2$, external analytical solution $\lambda_1 = 10^3, \lambda_2 = 10^{-3}$	5.125
model SC1c	$[0, 50] \times [6, 100]$	200×400	$\alpha_{\text{trunc}} = 0.1$, external analytical solution $\lambda_1 = 10^3, \lambda_2 = 10^{-3}$	4.875
model SC1d	$[0, 50] \times [6, 100]$	200×400	$\alpha_{\text{trunc}} = 0.01$, external analytical solution $\lambda_1 = 10^3, \lambda_2 = 10^{-3}$	3.625
model SC1e	$[0, 50] \times [6, 100]$	200×400	$\alpha_{\text{trunc}} = 0.001$, external analytical solution $\lambda_1 = 10^3, \lambda_2 = 10^{-3}$	2.625
model SC2	$[0, 50] \times [6, 100]$	200×400	$\alpha_{\text{trunc}} = 0.4$, external analytical solution $\lambda_1 = 100, \lambda_2 = 0.1$	5.375
model SC3	$[0, 50] \times [6, 100]$	200×400	same as model SC2, but solutions are swapped	5.375
model SC4	$[0, 50] \times [6, 100]$	200×400	$\alpha_{\text{trunc}} = 0.4$, external analytical solution $\lambda_1 = 1, \lambda_2 = 0.1$	5.375
model SC5	$[0, 50] \times [6, 100]$	200×400	same as model SC4, but solutions are swapped	5.375
model SC1f	$[0, 50] \times [6, 100]$	200×400	$\alpha_{\text{trunc}} = 0.0005$, external analytical solution $\lambda_1 = 10^3, \lambda_2 = 10^{-3}$	2.375
model SC1g	$[0, 10] \times [6, 20]$	200×400	$\alpha_{\text{trunc}} = 1 \times 10^{-5}$, external analytical solution $\lambda_1 = 10^3, \lambda_2 = 10^{-3}$	0.575

previous paper (Stute et al. 2008, Paper I hereafter), wherein we presented numerical simulations of truncated flows whose initial conditions are based on analytical self-similar models.

In order to test our truncated models, we will now apply our simulations to observations. In recent years, many NIR and optical data have become available exploring the morphology and kinematics of the jet launching region (e.g. Dougados et al. 2000; Ray et al. 2007; Dougados 2008, and references therein). Hubble Space Telescope (HST) and adaptive optics (AO) observations give access to the innermost regions of the wind, where the acceleration and collimation occurs (Ray et al. 1996; Dougados et al. 2000; Woitas et al. 2002; Hartigan et al. 2004). Because YSO jets emit in a number of atomic (and molecular) lines, we used a set of tools described in Gracia et al. (in prep.) to create emission maps in different forbidden lines which were used by other authors to extract the jet width from images. The observed jet widths will be compared with those extracted from our synthetic images. A similar study has been done by Cabrit et al. (1999), Garcia et al. (2001) and Dougados et al. (2004) using a different set of semi-analytical self-similar disk-jet solutions from Ferreira (1997) and Casse & Ferreira (2000a). Observed jet widths could be reproduced by manually truncating the solutions inside 0.07 AU and outside 1 AU, but the modification of flow streamlines induced by truncation was ignored.

The remainder of the paper is organized as follows: we briefly review the initial setup of the numerical simulations in Sect. 2 and describe our procedure for the comparison with observations in Sect. 3. The results of our studies are presented in Sects. 4–6. Finally, we conclude with the implications of the results in terms of the structure of the disk and the respective launching radii of the jets in YSOs.

2. Initial model setup and numerical simulations

This work is based on the results of our numerical simulations discussed in our paper I and two new models. We solved the MHD equations with the PLUTO code¹ (Mignone et al. 2007) starting from an initial condition set according to a steady, radially self-similar solution as described in V00, hereafter labelled ADO (*analytical disk outflow solution*, as in M08), which crosses all three critical surfaces. At the symmetry axis, the analytical solution was modified as described in GVT06 and M08.

To study the influence of the truncation of the analytical solution, we divided our computational domain into a jet region and an external region, separated by a truncation field line α_{trunc} . For lower values of the normalized magnetic flux

function, i.e. $\alpha < \alpha_{\text{trunc}}$ – or conversely smaller cylindrical radii – our initial conditions are fully determined by the solution of V00 and the modification of GVT06 and M08 close to the axis. In the outer region we modified all quantities and initialized them with another analytical solution, but with modified parameters. From V00, one can show that if we start with an arbitrary MHD solution with the variables $\rho, p, \mathbf{v}, \mathbf{B}$, one can easily construct a second solution by using two free parameters² λ_1 and λ_2 , with $\rho' = \lambda_1 \lambda_2^2 \rho, p' = \lambda_2^2 p, \mathbf{B}' = \lambda_2 \mathbf{B}$ and $\mathbf{v}' = \lambda_1^{-1/2} \mathbf{v}$. Thus some or all quantities are scaled down in the external region depending on our choice of parameters. In Table 1 we give the parameters of the models (some of which we studied in Paper I as well as new ones) used in this study.

For further details, we refer the reader to Paper I.

3. Comparison of synthetic emission runs with observations

Numerical simulations and observations cannot be directly compared. While the former describe the plasma in terms of physical quantities like density, pressure, magnetic field and velocities, the latter observes only photon flux as a function of frequency. This comparison can be facilitated by means of constructing synthetic maps. However, translating numerical simulations into such synthetic maps is very complicated. In general, the local emissivity is a function of temperature, electron density and density of the respective ion, as e.g., n_{OH} for singly ionized oxygen. The emissivities are integrated along a given line-of-sight and projected onto the plane of the sky producing an ideal synthetic emission map. Finally, real detectors distort this ideal map through their detector response, which needs to be taken into account.

In this paper, we use the set of tools OpenSESAME³ v0.1 described in Gracia et al. (in prep.) to produce synthetic observations from our simulations in different consecutive stages. The first stage approximates the ionization state of each atom by locally solving a chemical network under the assumption of local equilibrium. The second stage calculates the statistical equilibrium of level populations for each ion of interest as a function of temperature and density and yields the emissivity for individual transitions of interest. Further stages take care of integration along the line-of-sight and projection. Finally, the

² Strictly speaking this is only true when all lengths are also scaled, but because only the gravity term explicitly depends on the length scale and in our case the gravitational force is small compared to the other forces, this slight inconsistency is unimportant (see Paper I).

³ <http://homepages.dias.ie/~jgracia/OpenSESAME/>

¹ <http://plutocode.to.astro.it/>

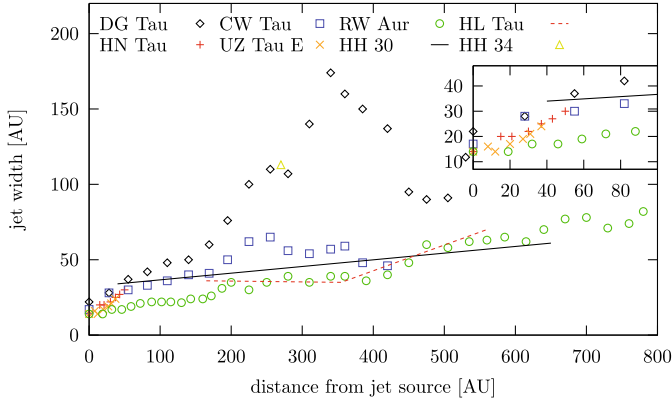


Fig. 1. Variation of jet width ($FWHM$) derived from [SII] and [OI] images as a function of distance from the source. Data points are from CFHT/PUEO and HST/STIS observations of DG Tau (diamonds), HN Tau (plus signs), CW Tau (squares), UZ Tau E (crosses), RW Aur (circles), HH 34 (one triangle), HH 30 (black solid line) and HL Tau (red dashed line); data are taken from Ray et al. (2007) and references therein.

ideal maps are convolved with a Gaussian point-spread-function (PSF) to mimic the finite spatial resolution of a given instrument. These synthetic emission maps are then quantitatively analyzed with similar techniques used on real observed maps. We refer to “runs” as runs of OpenSESAME with different sets of scalings (see below) and to “models” as different MHD simulations with PLUTO (Table 1).

We compare the width of jets measured from HST and AO observations (Dougados et al. 2000; Ray et al. 2007; Dougados 2008, and references therein) with the width from synthetic emission maps calculated from our MHD models. We convolved the maps with a Gaussian with a full-width half-maximum ($FWHM$) of 15 AU ($\sigma = 6.37$ AU) throughout this paper, equivalent to HST’s resolution of $0.1''$ at a distance of 150 pc. We use a sample of eight jets: DG Tau, HN Tau, CW Tau, UZ Tau E, RW Aur, HH34, HH30 and HL Tau (Fig. 1). In order to determine the width of the jets in our models, we use a method which is as close as possible to that applied by the observers. We create convolved synthetic maps for the emission in the [SII] $\lambda 6731$ and [OI] $\lambda 6300$ lines for each numerical model and each run of OpenSESAME and determine the jet width from the map’s $FWHM$ as a function of distance along the axis.

3.1. Normalizations

Throughout the first paper, we used only the dimensionless quantities in which PLUTO performs its calculations. In order to compare our results with observations, however, i.e. in order to run OpenSESAME correctly, we have to scale them to physical units by providing scaling factors for density ρ_0 , pressure p_0 , velocity v_0 , magnetic field strength B_0 , a length scale R_0 and a mass scale M . However, in terms of the normalizations used in the PLUTO code, only three of those quantities are independent. A possible choice is the mass of the central object, velocity scale and density scale, while the remaining factors are calculated from these.

Here we use three different “coordinate systems”: i) the computational grid of cells with indices (i, j) from $(0, 0)$ to $(199, 399)$, ii) the PLUTO domain from $(0, 6)$ to $(50, 100)$ and iii) the physical scale of the jet in AU, which is simply the PLUTO domain

multiplied with a length scale R_0 . In the solution of V00, the length scale R_0 is connected to the mass of the central object and the velocity normalization via

$$R_0 = \frac{\mathcal{G} M}{4 v_0^2} = 110.9 \text{ AU} \left(\frac{v_0}{\text{km s}^{-1}} \right)^{-2} \left(\frac{M}{0.5 M_\odot} \right). \quad (1)$$

From the velocity and density normalization directly follow the normalizations for the magnetic field and pressure as

$$p_0 = \rho_0 v_0^2 = 10^{-11} \text{ g cm}^{-1} \text{ s}^{-2} \left(\frac{\rho_0}{10^{-21} \text{ g cm}^{-3}} \right) \left(\frac{v_0}{\text{km s}^{-1}} \right)^2, \quad (2)$$

$$B_0 = \sqrt{4 \pi \rho_0 v_0^2} = 11.21 \mu\text{G} \left(\frac{\rho_0}{10^{-21} \text{ g cm}^{-3}} \right)^{1/2} \left(\frac{v_0}{\text{km s}^{-1}} \right). \quad (3)$$

The mass of the central object affects only the length scale. The pressure and temperature of the jet and thus the synthetic emission maps are affected only by the unit density and unit velocity.

As typical jet velocities in YSOs we assumed values of 100, 300, 600 and 1000 km s^{-1} , as typical masses of T Tauri stars 0.2, 0.5 and 0.8 M_\odot (Hartigan et al. 1995), and as jet number densities values of 125, 500, 1000 and $5 \times 10^4 \text{ cm}^{-3}$. We adopt the nomenclature for our runs as e.g. $(n_{\text{jet}}, v_{\text{jet}}, M)$ with n_{jet} in cm^{-3} , v_{jet} in km s^{-1} and M in M_\odot .

In order to find the normalizations listed above, we needed to have typical values of jet density and velocity at a certain position (R, z) for a given mass M , and iteratively solved the Eq. (1). Details of this algorithm and also a graphical picture of this approach are given in Appendix A. The normalizations vary from numerical model to numerical model, therefore we used the corresponding different values for each model.

As another constraint, we require that R_0 is small enough that the $FWHM$ of the Gaussian of 15 AU is sampled by a reasonable number of pixels. Because the resolution of our numerical simulations was four pixels per R_0 , requiring at least two pixels per $FWHM$ requires $R_0 < 30$ AU. This limit highly reduces the number of runs, from 576 to 180. The only valid runs are

- $(\dots, 600, 0.2)$, $(\dots, 600, 0.5)$, $(\dots, 1000, 0.5)$, $(\dots, 1000, 0.8)$ for models ADO, SC1a–b, SC2, SC4;
- $(\dots, 600, 0.2)$, $(\dots, 600, 0.5)$, $(\dots, 1000, 0.2)$, $(\dots, 1000, 0.5)$, $(\dots, 1000, 0.8)$ for models SC1c–f;
- $(\dots, 600, 0.2)$, $(\dots, 1000, 0.2)$, $(\dots, 1000, 0.5)$, $(\dots, 1000, 0.8)$ for model SC1g;
- $(\dots, 100, 0.2)$ for model SC3;
- no valid runs for model SC5.

The corresponding values of R_0 are listed in Table 2.

3.2. The artefact of limb-brightening

After plotting transverse intensity cuts through the convolved emission maps, it can be seen that the maximum emission does not come from the axis, but from a small shell at a finite radius (Fig. 2, left). This effect of limb-brightening, which has been never observed up to now in real protostellar jets, is a direct consequence of the density and pressure/temperature profiles in the analytical solution and is present in all our models and runs, the untruncated model ADO as well as our truncated models. Details of the physical reasons for this behavior are given in Appendix B.

Because the analytical solution is not well defined close to the axis and we had to interpolate it in our numerical simulations, and because it is likely that a stellar wind resides inside

Table 2. R_0 in AU of the different OpenSESAME runs.

Model	($\dots, 600, 0.2$)	($\dots, 600, 0.5$)	($\dots, 1000, 0.2$)	($\dots, 1000, 0.5$)	($\dots, 1000, 0.8$)
ADO	1.20	7.60	–	1.04	2.47
SC1a	2.32	7.60	–	1.98	2.99
SC1b	2.17	7.59	–	1.98	3.33
SC1c	2.40	7.60	0.98	2.19	3.47
SC1d	2.91	8.87	1.34	2.61	4.10
SC1e	4.54	13.96	2.06	4.22	5.86
SC1f	5.29	14.40	2.17	4.86	6.91
SC1g	8.03	–	3.04	7.23	13.69
SC2	2.31	7.60	–	1.96	2.98
SC4	2.05	7.60	–	2.08	2.97
Model	($\dots, 100, 0.2$)				
SC3	0.97				

the disk wind (Matsakos et al. 2009), we applied the following corrections before running OpenSESAME:

- we *limited* the temperature to 10^4 K in the whole domain;
- we limited the density around the axis by setting the density inside 1 *FWHM* to its value at 1 *FWHM* for each z .

This value of T is typical of that deduced from analyses of line ratios in jets (e.g. Bacciotti & Eisloffel 1999; Lavalley-Fouquet et al. 2000). The artefact of limb-brightening is removed by limiting T . For numerical reasons, the density shows a steep increase close to the jet axis. This artefact has to be corrected to obtain jetwidths above 1 *FWHM*.

4. Do we have to truncate the disk?

Before we present the implications of truncating the analytical solution below, we have to compare the unmodified ADO solution (Vlahakis et al. 2000) with observations to show that the truncation is indeed needed. Figure 3 shows the typical output of OpenSESAME: cuts of the density and temperature, the electron and SII and OI ion densities and synthetic emission maps of the [SII] $\lambda 6731$ and [OI] $\lambda 6300$ lines, all for model ADO and run (500, 600, 0.5). The electron density shows a steep cut-off along a field line anchored at about $5 R_0$ where the temperature drops below 10^4 K, while the [SII] and [OI] emission maps show a somewhat shallower cut-off, which is located at a larger radius (about $8 R_0$). Synthetic emission maps of the [OI] $\lambda 6300$ line for all models and runs are shown in Appendix C.

The extracted jet widths in normalized R_0 units are plotted in Fig. 4. In each plot we combine runs with equal velocities and masses, i.e. only varying the density, which result in identical jet widths as expected. Because we extracted the jet width from a *ratio* of intensities by using the *FWHM* (we divided the maps by the intensity on the axis and check where the ratio is 0.5), the factor ρ^2 cancels out.

Much larger changes are present when we compare runs where ρ_0 is identical, but v_0 varies (top right and bottom left plot) and when we look for the influence of the mass (plots in each row). The jet widths derived from synthetic [OI] are identical to those derived from synthetic [SII] images, thus we show only results based on [OI] images.

The jet widths in R_0 increase with increasing velocity. A higher mass reduces the normalized jet width considerably. In run (500, 600, 0.5), as seen in Fig. 3, the extracted jet width does not follow any directly apparent feature in the emissivity maps nor a specific contour line.

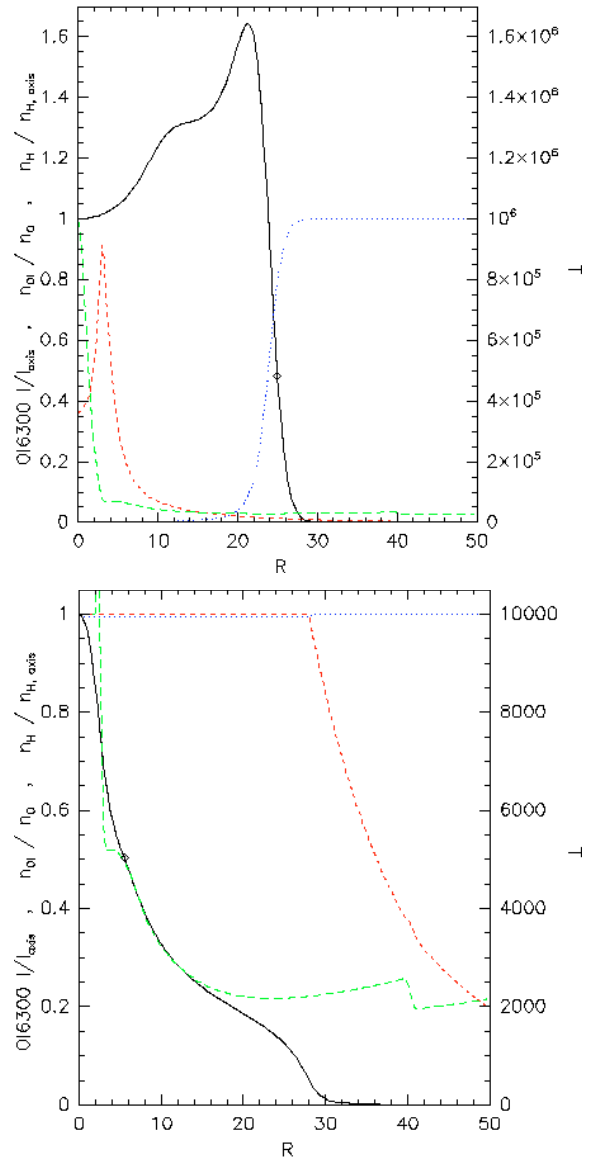


Fig. 2. Transverse intensity cuts of the convolved [OI] $\lambda 6300$ emission at $z = 100$ AU (black, solid), normalized to its value on the axis, for model ADO and run (500, 600, 0.5); without corrections of density and temperature they show the effect of limb-brightening (*top*) which vanishes after the corrections (*bottom*); also plotted are cuts of the normalized hydrogen number density (long-dashed, green), of $n_{\text{OI}}/n_{\text{O}}$ (blue, dotted) and of the temperature (dashed, red, y -axis on the *right-hand side*). $R_0 = 7.60$ AU.

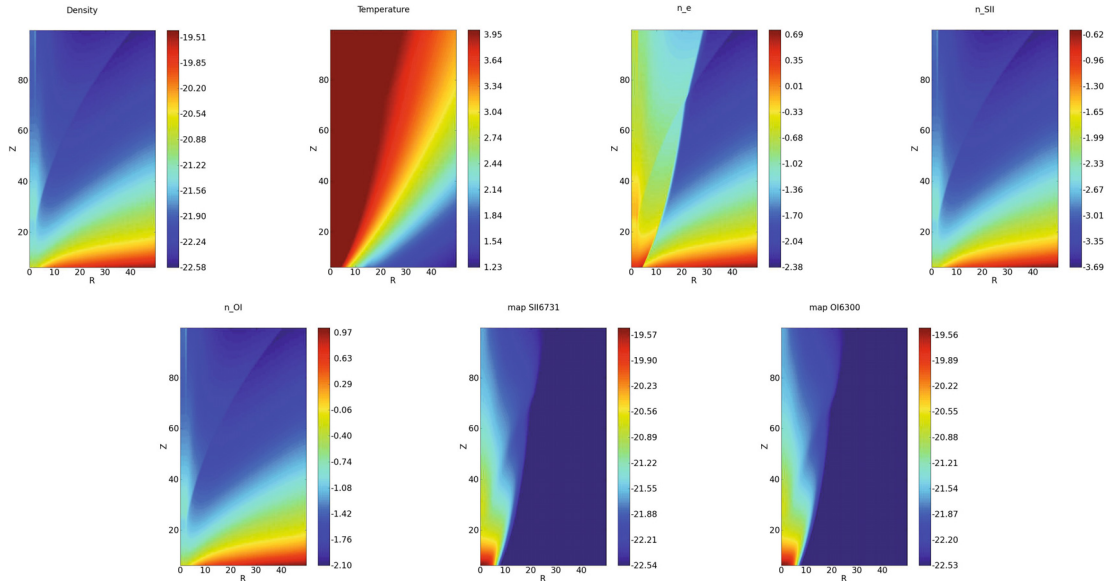


Fig. 3. Typical output of OpenSESAME: cuts of the density and temperature, the electron and SII and OI ion densities and synthetic emission maps of the [SII] $\lambda 6731$ and [OI] $\lambda 6300$ lines for model ADO and run (500, 600, 0.5). $R_0 = 7.60$ AU.

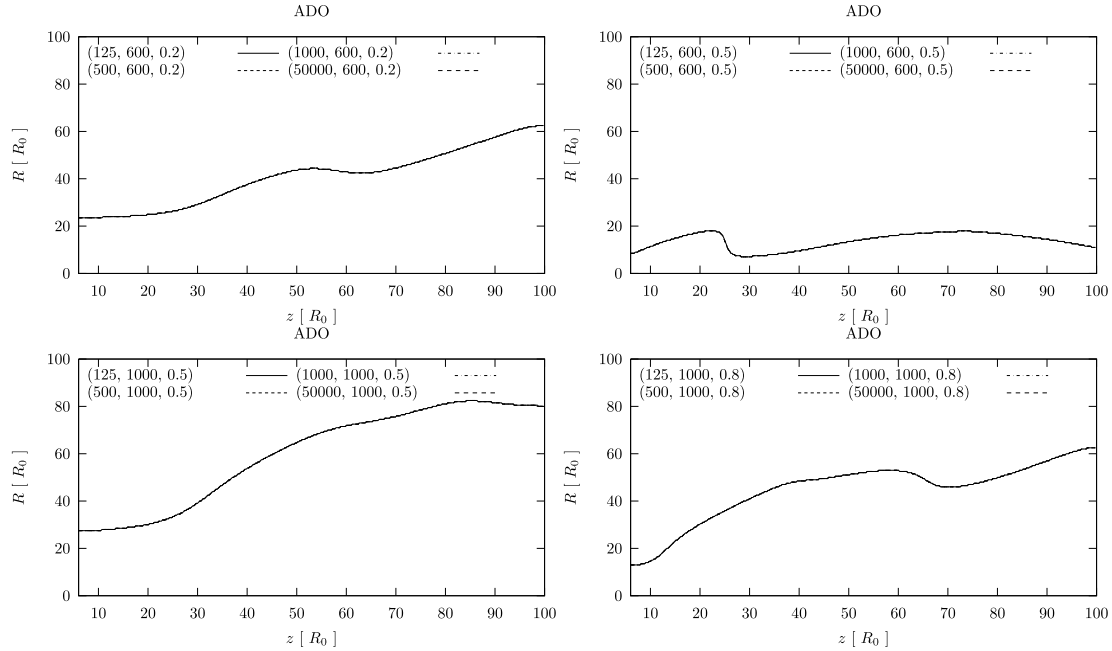


Fig. 4. Dimensionless jet width derived from synthetic [OI] images as a function of distance from the source in model ADO.

After rescaling the jet widths with the appropriate values of R_0 , we compared the modeled and observed jet widths in AU (Fig. 5). The jet widths are now rescaled with R_0 , which is proportional to the mass and anti-proportional to v_0 (Eq. (1)). Because $f(i) \equiv v_{\text{jet}}/v_0$ is almost constant in our range of R_0 , v_{jet} and v_0 can be interchanged. This behavior of R_0 is now dominant, thus the jet width increases with increasing mass and decreases with increasing jet velocity, although the second effect seems to be of minor importance.

The untruncated ADO model on average gives too large jet widths compared to the observations of T Tauri jets. The first five data points within 120 AU from the jet source in DG Tau can be best approximated with run (500, 600, 0.2), unfortunately our model does not provide results farther out for such a small R_0 . At distances above 200 AU, the run (500, 600, 0.5) gives a jet

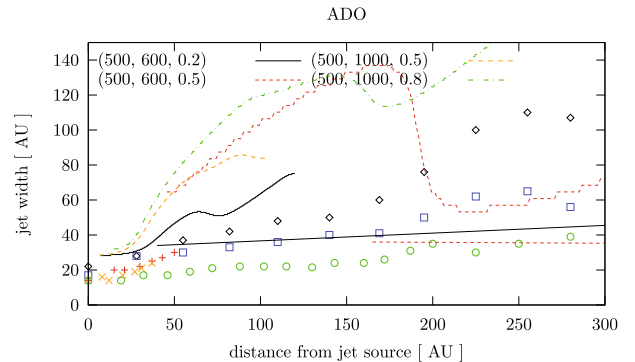


Fig. 5. Jet widths in AU derived from synthetic [OI] images as a function of distance from the source in model ADO; overlaid are the data points of Fig. 1.

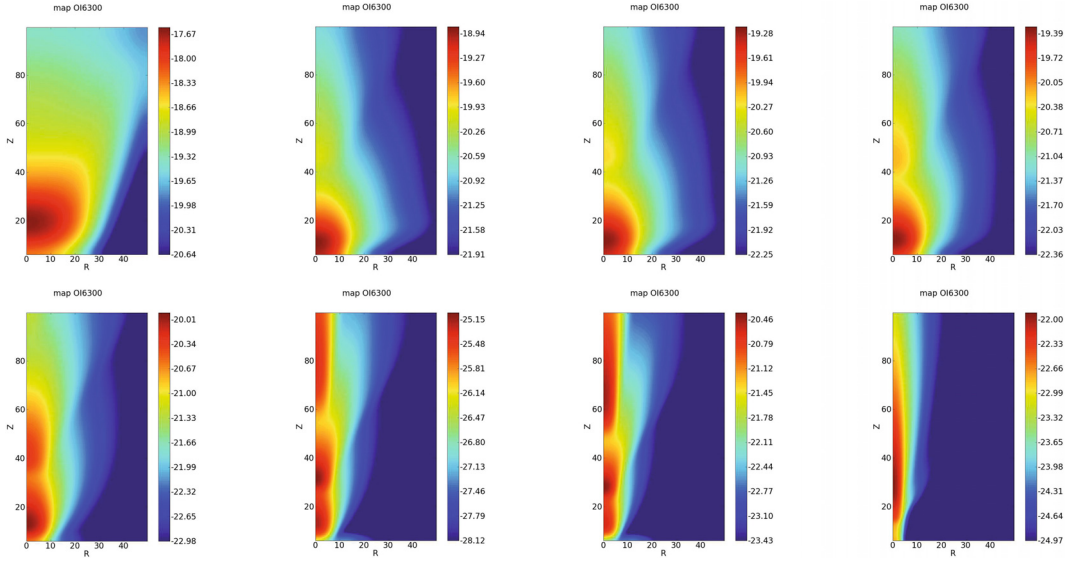


Fig. 6. Synthetic emission maps of the [OI] $\lambda 6300$ line, convolved with a Gaussian PSF with a $FWHM$ of 15 AU, for run (500, 1000, 0.5). *Top row:* models ADO ($R_0 = 1.04$ AU), SC1a ($R_0 = 1.98$ AU), SC1b ($R_0 = 1.98$ AU), SC1c ($R_0 = 2.19$ AU); *bottom row:* models SC1d ($R_0 = 2.61$ AU), SC1e ($R_0 = 4.22$ AU), SC1f ($R_0 = 4.86$ AU), SC1g ($R_0 = 7.23$ AU).

width in the observed range but only after the first bump, which is intrinsic for our analytical model. Hartigan et al. (1995) give a mass of DG Tau of $0.67 M_{\odot}$, i.e. higher than in both models. Although this difference in mass might not be meaningful, we conclude that to be able to reproduce all jets in our sample, we need an additional effect which reduces the derived jet width.

5. Effects of outer truncation

First we investigate the effects of outer truncation. Convolved synthetic maps for the emission in [OI] $\lambda 6300$ for some numerical models and run (500, 1000, 0.5) are given in Fig. 6. Truncation leads to collimation of the emission region with respect to the model ADO without any truncation.

Again we extracted the jet width from emission maps like these. The resulting widths derived from the synthetic [OI] images and scaled to AU are presented in Fig. 7. We found similarities in behavior in the truncated models to the untruncated model ADO. The jet widths show again no dependency on the density, as described for model ADO in the previous section. Surprisingly, in models SC1a-c, SC2 and SC4 the runs (500, 600, 0.2) and (500, 1000, 0.5) and also (500, 1000, 0.8) lead to almost similar physical jet widths. The first two also almost coincide in models SC1d-e. As in model ADO, also in the truncated models the run (500, 600, 0.5) has the smallest jet widths (after the first bump). In principle, we can reproduce even smaller values than the observed ones.

6. Effects of inner truncation

In Paper I we also performed numerical simulations, in which we truncated the analytical solution in the interior, i.e. at an inner truncation radius. The physical picture behind this scenario is a stellar magnetosphere truncating the jet-emitting disk. We showed that inner truncation leads to a decrease of the jet radius and compression of the material in the inner region. Unfortunately, only one run met our scaling requirements (Sect. 3.1): model SC3 and run (\dots , 100, 0.2). For this model, a convolved synthetic map for the emission in [OI] $\lambda 6300$ is given in Fig. 8.

After rescaling the derived jet width to AU, we found an almost constant width in the range of the observed values. Note that our model does not provide results farther out than 100 AU due to a small R_0 .

7. Discussion

We studied the jet widths derived from synthetic emission maps in different forbidden lines as the full-width half-maximum of the emission.

We found that the untruncated model ADO of Vlahakis et al. (2000) cannot account for the small jet widths found in recent optical images taken with HST and AO. The density normalization is not important for the resulting measured jet width as long as we are far from the critical regime.

We investigated different effects for reducing the derived jet width: by imposing an outer radius of the launching region of the underlying accreting disk and thus also of the outflow on the observable structure of the jet and by imposing an inner radius of the underlying accretion disk due to interactions with the stellar magnetosphere.

7.1. Outer truncation

We created synthetic images based on our simulations of truncated disk winds (Stute et al. 2008) as well as new simulations and found that the extracted jet widths in the truncated models decrease for models SC1a–1g, compared to those of the untruncated model ADO, as naively expected.

In the present paradigm, jets are emitted only by the inner part of the disk. Hence in the other parts the disk can be described by a standard accretion disk (SAD), in the inner parts by a jet-emitting disk (JED). Anderson et al. (2003) showed that one can estimate the launching region as

$$R_0 = 0.24 \text{ AU} \left(\frac{R_{\infty}}{70 \text{ AU}} \right)^{2/3} \left(\frac{v_{\phi, \infty}}{10 \text{ km s}^{-1}} \right)^{2/3} \times \left(\frac{v_{p, \infty}}{500 \text{ km s}^{-1}} \right)^{-4/3} \left(\frac{\mathcal{M}}{0.5 M_{\odot}} \right)^{1/3}.$$

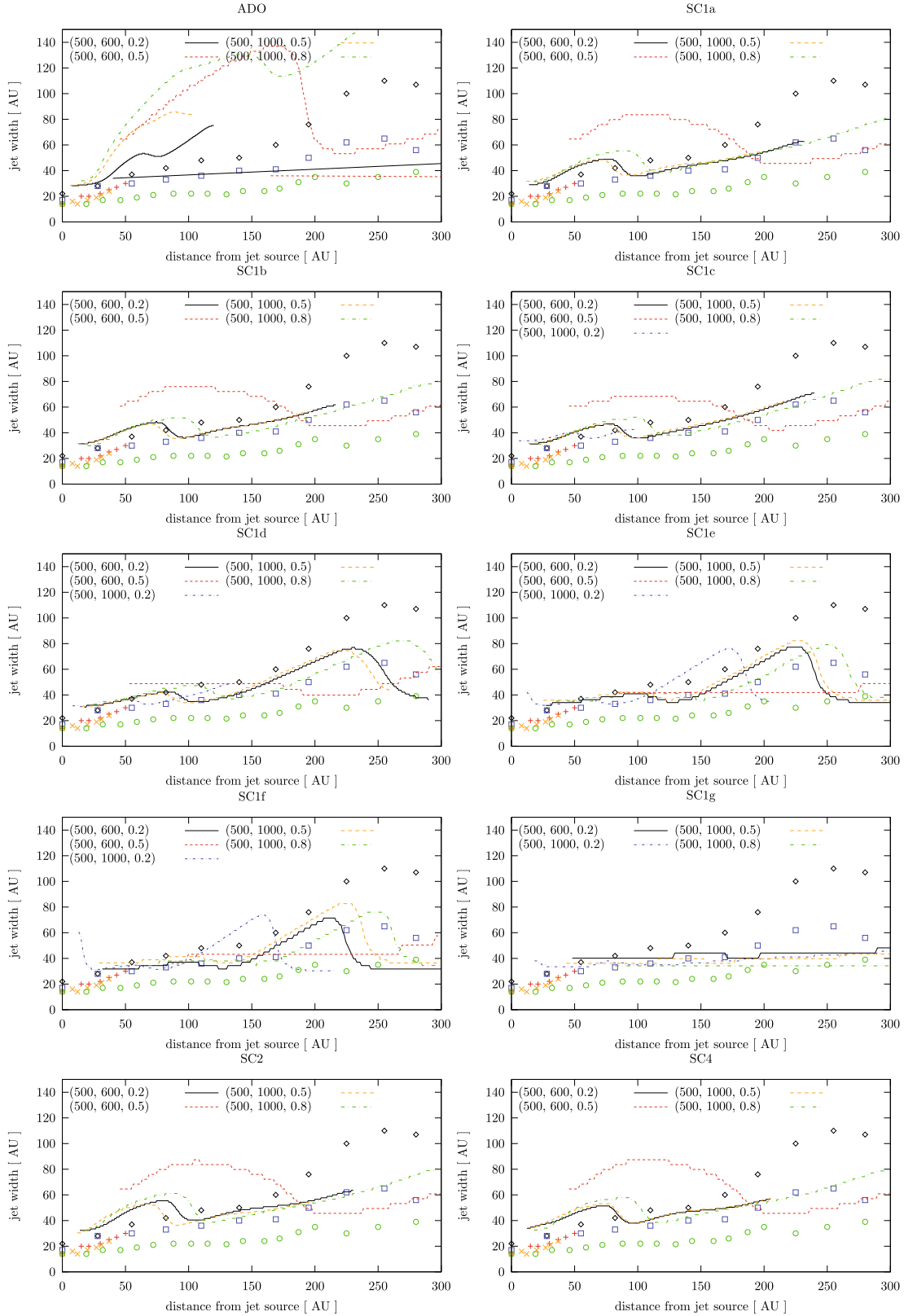


Fig. 7. Jet widths in AU derived from synthetic [OI] images as a function of distance from the source in models ADO and SC1a–g, SC2 and SC4 and for runs (500, 600, 0.2), (500, 600, 0.5), (500, 1000, 0.5), (500, 1000, 0.8); overlaid are the data points of Fig. 1.

This transition was constrained observationally with measured jet rotation velocities and using the equation above and radii of the order of 0.1–1 AU are used in several theoretical studies as e.g. [Combet & Ferreira \(2008\)](#).

Our results can be used to infer the “real” value of the truncation radius R_{trunc} in the observed sample of jets and interpret it as the transition radius of the JED to the SAD, assuming the specific model of V00 applies.

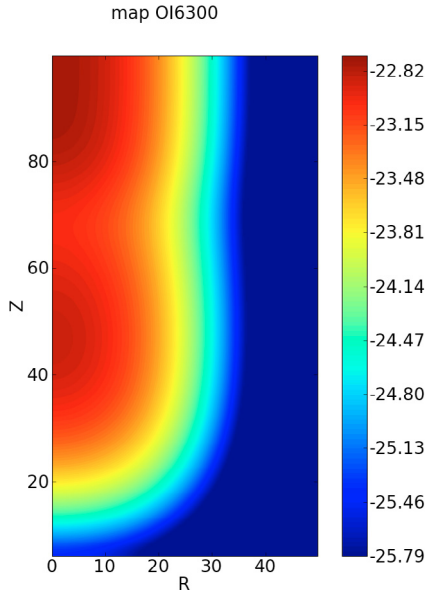


Fig. 8. Synthetic emission maps of the [OI] $\lambda 6300$ line, convolved with a Gaussian PSF with a $FWHM$ of 15 AU, for model SC3 and run $(\dots, 100, 0.2)$. $R_0 = 0.97$ AU.

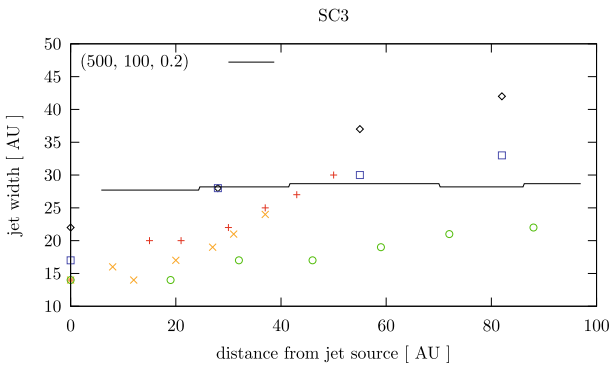


Fig. 9. Jet widths in AU derived from synthetic [OI] images as a function of distance from the source in model SC3 and for run $(500, 100, 0.2)$; overlaid are the data points of Fig. 1.

At the lower boundary in our simulations, the truncation radii are given in Table 1. They vary from $5.375 R_0$ in model SC1a to $0.575 R_0$ in model SC1g. However, these radii are set at $z = 6 R_0$ (the lower boundary), not in the equatorial plane. Those can be calculated by extrapolating the field line, i.e.

$$R_{\text{trunc}|z=0} = R_{\text{trunc}|z=6} \frac{G(\pi/2)}{G(\theta_{\text{trunc}})}, \quad (4)$$

with $\theta_{\text{trunc}} = \arctan(R_{\text{trunc}|z=6}/6)$ and G taken from the analytical solution of V00. This gives the following results:

- in models SC1a, SC2–4 $R_{\text{trunc}|z=0} = 0.11316 R_0$,
- in model SC1b $R_{\text{trunc}|z=0} = 0.09099 R_0$,
- in model SC1c $R_{\text{trunc}|z=0} = 0.07275 R_0$,
- in model SC1d $R_{\text{trunc}|z=0} = 0.0213 R_0$,
- in model SC1e $R_{\text{trunc}|z=0} = 0.00722 R_0$,
- in model SC1f $R_{\text{trunc}|z=0} = 0.00546 R_0$ and
- in model SC1g $R_{\text{trunc}|z=0} = 0.00069 R_0$.

The last step is a multiplication with R_0 of the best-fit model (Table 2). The resulting values of $R_{\text{trunc}|z=0}$ in AU for each model and run are given in Table 3.

We found best-fit models for the jets in the observed sample. Note that we always ignored the first bump in the synthetic jet widths and focussed on larger distances from the source:

- the observed mass of DG Tau (diamonds in Fig. 7) is $0.67 M_\odot$ (Hartigan et al. 1995), therefore we have to focus on the runs $(500, 1000, 0.8)$, and perhaps also runs $(500, 600, 0.5)$ and $(500, 1000, 0.5)$. The best-fit model is between ADO and SC1a, thus the truncation radius is larger than 0.22 AU;
- HN Tau (plus signs) has a mass of $0.72 M_\odot$ (Hartigan et al. 1995), thus again the runs $(500, 1000, 0.8)$ are favored. Because we ignored the first bump, we interpolated the jet shape at larger distances and found a best-fit model between ADO and SC1a, thus the truncation radius is again larger than 0.34 AU. However, this result is highly uncertain;
- the mass of CW Tau (squares) is the highest in our sample, $1.03 M_\odot$ (Hartigan et al. 1995). Using the runs $(500, 1000, 0.8)$, the best-fit model is SC1b or SC1c. The truncation radius is thus between 0.25 – 0.3 AU;
- UZ Tau E (crosses) has the lowest mass in our sample, only $0.18 M_\odot$ (Hartigan et al. 1995), we use the runs $(500, 600, 0.2)$. Again we had to interpolate the jet width from larger distances and choose model SC1a as best-fit model. The truncation radius is about 0.26 AU;
- the measured mass of RW Aur (circles) is $0.85 M_\odot$ (Hartigan et al. 1995), thus we have to focus on runs $(500, 1000, 0.8)$. We need a very high degree of truncation as in models SC1e–g, thus a truncation radius of the order of 0.04 AU.

7.2. Inner truncation

Because the jet-emitting accretion disk is thought to be truncated by the stellar magnetosphere, we also investigated our models in which the analytical solution is truncated at an inner radius. We found that inner truncation can also reduce the extracted jet widths. The jet width from our model SC3 and run $(\dots, 100, 0.2)$ is about 30 AU for the inner 100 AU of the jet. This is well in the observed range of 15 – 45 AU. Because we did not vary the inner truncation radius, we can only claim – based on our results of Paper I – that the larger the truncation radius, the higher is the compression of the resulting jet. In our models we chose a radius of $5.375 R_0$ at $z = 6$. For model SC3 and run $(\dots, 100, 0.2)$, this corresponds to an inner truncation radius of 0.11 AU, which is only slightly higher than the inner hole in T Tauri disks (0.02 – 0.07 AU, Najita et al. 2007). A parameter study varying the inner truncation radius is needed.

8. Conclusions

We showed as a proof of concept that jet widths derived from numerical simulations extending analytical MHD jet formation models can be very helpful for understanding recently observed jet widths from observations with adaptive optics and space telescopes. However, further aspects have to be investigated in more detail.

An intrinsic feature in all our models with outer truncation is the first bump in the extracted jet width, which complicates the comparison of synthetic and observed jet widths. Only for DG Tau and CW Tau, we could unambiguously find models with outer truncation which fitted the observed jet widths at larger distances. For HN Tau and UZ Tau E, we have no observed jet widths at larger distances, only in the region which is contaminated by the bump. RW Aur shows very small observed jet widths at all scales, which cannot be reproduced by any of our

Table 3. Truncation radius at the equator $R_{\text{trunc}|z=0}$ in AU of the different OpenSESAME runs.

Model	($\dots, 600, 0.2$)	($\dots, 600, 0.5$)	($\dots, 1000, 0.2$)	($\dots, 1000, 0.5$)	($\dots, 1000, 0.8$)
SC1a	0.263	0.860	–	0.224	0.338
SC1b	0.197	0.691	–	0.180	0.303
SC1c	0.175	0.553	0.071	0.159	0.252
SC1d	0.062	0.189	0.029	0.056	0.087
SC1e	0.033	0.101	0.015	0.030	0.042
SC1f	0.029	0.079	0.012	0.027	0.038
SC1g	0.006	–	0.002	0.005	0.009
SC2	0.261	0.860	–	0.222	0.337
SC4	0.232	0.860	–	0.235	0.336
Model	($\dots, 100, 0.2$)				
SC3	0.11				

models and runs. The derived truncation radii (>0.25 AU) are several times larger than the inner radius of the gaseous disk in T Tauri stars (0.02–0.07 AU, Najita et al. 2007), thus our use of a self-similar disk-wind solution is consistent.

The model with inner truncation gives a synthetic jet width, which is constant and is within the range of observed widths. Another advantage of this model is that its flow velocities of the order of 100 km s^{-1} are closer to observed values. All models with outer truncation have very high velocities ($>600 \text{ km s}^{-1}$ at our scaling point of $R_{\text{jet}} = 10 \text{ AU}$ and $Z_{\text{jet}} = 100 \text{ AU}$), several times higher than in that with inner truncation.

Because we originally focused only on the effect of outer truncation, we kept the inner truncation radius constant in our models SC3 and SC5. In order to further explore the ability of inner truncation to reproduce the observations, we have to vary the inner truncation radius in a parameter study. Naively, one would expect that the derived jet widths are not decreasing for decreasing truncation radii as for the outer truncation, but are *increasing*. This, however, has to be tested with new simulations.

In our study, we assumed an inclination of 90° of the jet, thus projection effects may slightly change our results. We will present the results of such a study in a forthcoming paper.

Garcia et al. (2001) showed in their Fig. 1 that the measured jet widths are mainly characterized by the ejection index ξ , defined by Ferreira (1997). This is related to the model parameter x of the solution of V00, $\xi = 2(x - 3/4)$, and because in our simulations $x = 0.75$, we get $\xi = 0$, which is intrinsic for a standard disk. In the solution of Ferreira (1997), ξ also controls the opening of the field lines, because it is connected to the lever arm λ by $\lambda = 1 + 1/(2\xi)$. Garcia et al. (2001) favored cold solutions with values of λ between 50–70. If heating along streamlines is allowed, the relation is broken and also warm solutions of e.g. Casse & Ferreira (2000b) with smaller λ values of 8 and opening of streamlines (the ratio of the maximum radius to the initial launch radius) of about 30 can reproduce the observation. In the solution of V00, we have $\lambda = G(\pi/2)^{-2} \approx 39$ and the maximum opening $G_{\text{max}}/G(\pi/2) \approx 893$. The use of other solutions will therefore highly influence our results in terms of the outer truncation radius.

Acknowledgements. The authors would thank the referee, Sylvie Cabrit, for fruitful discussions, suggestions and comments improving this paper. The present work was supported in part by the European Community's Marie Curie Actions – Human Resource and Mobility within the JETSET (Jet Simulations, Experiments and Theory) network under contract MRTN-CT-2004 005592.

References

- Anderson, J. M., Li, Z.-Y., Krasnopolsky, R., & Blandford, R. D. 2003, *ApJ*, 590, L107
- Bacciotti, F., & Eisloffel, J. 1999, *A&A*, 342, 717
- Blandford, R. D., & Payne, D. G. 1982, *MNRAS*, 199, 883
- Cabrit, S., Edwards, S., Strom, S. E., & Strom, K. M. 1990, *ApJ*, 354, 687
- Cabrit, S., Ferreira, J., & Raga, A. C. 1999, *A&A*, 343, L61
- Casse, F., & Ferreira, J. 2000a, *A&A*, 353, 1115
- Casse, F., & Ferreira, J. 2000b, *A&A*, 361, 1178
- Combet, C., & Ferreira, J. 2008, *A&A*, 479, 481
- Dougados, C., Cabrit, S., Lavalley, C., & Menard, F. 2000, *A&A*, 357, L61
- Dougados, C., Cabrit, S., Ferreira, J., et al. 2004, *Ap&SS*, 293, 45
- Dougados, C. 2008, in *Jets from Young Stars II: Clues from High Angular Resolution Observations*, ed. F. Bacciotti, E. Whelan, & L. Testi (Berlin Heidelberg: Springer-Verlag), Lecture Notes Phys., 742
- Ferreira, J. 1997, *A&A*, 319, 340
- Ferreira, J. 2007, in *Jets from Young Stars: Models and Constraints*, ed. J. Ferreira, C. Dougados, & E. Whelan (Berlin, Heidelberg: Springer-Verlag), Lecture Notes Phys., 723
- Garcia, P. J. V., Cabrit, S., Ferreira, J., & Binette, L. 2001, *A&A*, 377, 609
- Gracia, J., Vlahakis, N., & Tsinganos, K. 2006, *MNRAS*, 367, 201 (GVT06)
- Hartigan, P., Edwards, S., & Ghandour, L. 1995, *ApJ*, 452, 736
- Hartigan, P., Edwards, S., & Pierson, R. 2004, *ApJ*, 609, 261
- Hartmann, L. 2009, in *Protostellar Jets in Context*, ed. K. Tsinganos, T. P. Ray, & M. Stute (Berlin, Heidelberg: Springer-Verlag)
- Lavalley-Fouquet, C., Cabrit, S., & Dougados, C. 2000, *A&A*, 356, L41
- Livio, M. 2009, in *Protostellar Jets in Context*, ed. K. Tsinganos, T. P. Ray, & M. Stute (Berlin, Heidelberg: Springer-Verlag)
- Matsakos, T., Tsinganos, K., Vlahakis, N., et al. 2008, *A&A*, 477, 521, M08
- Matsakos, T., Massaglia, S., Trussoni, E., et al. 2009, *A&A*, 502, 217
- Mignone, A., Bodo, G., Massaglia, S., et al. 2007, *ApJS*, 170, 228
- Najita, J. R., Carr, J. S., Glassgold, A. E., & Valenti, J. A. 2007, in *Protostars and Planets V*, ed. B. Reipurth, D. Jewitt, & K. Keil (Tucson: University of Arizona Press), 507
- Ray, T. P., Mundt, R., Dyson, J. E., Falle, S. A. E. G., & Raga, A. C. 1996, *ApJ*, 468, L103
- Ray, T. P., Dougados, C., Bacciotti, F., et al. 2007, in *Protostars and Planets V*, ed. B. Reipurth, D. Jewitt, & K. Keil (Tucson: University of Arizona Press), 231
- Stute, M., Tsinganos, K., Vlahakis, N., Matsakos, T., & Gracia, J. 2008, *A&A*, 491, 339, Paper 1
- Tzeferacos, P., Ferrari, A., Mignone, A., et al. 2009, *MNRAS*, 400, 820
- Vlahakis, N., & Tsinganos, K. 1998, *MNRAS*, 298, 777
- Vlahakis, N., Tsinganos, K., Sauty, C., & Trussoni, E. 2000, *MNRAS*, 318, 417
- Woitas, J., Ray, T. P., Bacciotti, F., Davis, C. J., & Eisloffel, J. 2002, *ApJ*, 580, 336
- Zanni, C., Ferrari, A., Rosner, R., Bodo, G., & Massaglia, S. 2007, *A&A*, 469, 811

Appendix A: Details of the normalization algorithm

In order to find the reference values for the distance R_0 , pressure p_0 and magnetic field B_0 listed in Eqs. (1)–(3), we require some typical values of jet density and velocity at a certain

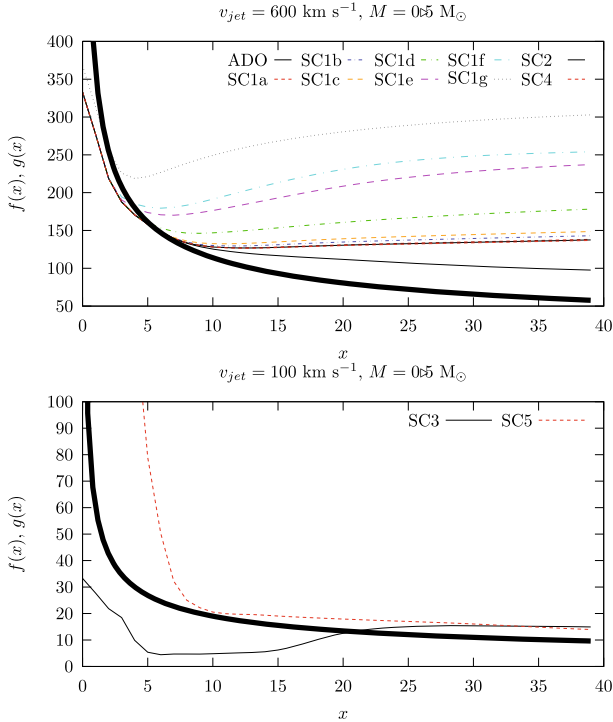


Fig. A.1. Shape of the functions $f(i)$ for all models and of the function $g(i)$ (thick curve) for $v_{jet} = 600 \text{ km s}^{-1}$ (100 km s^{-1} for the models with inner truncation in the *bottom panel*) and $M = 0.5 M_{\odot}$.

position – we define the jet as the region at the physical position $(R_{jet}, z_{jet}) = (10, 100) \text{ AU}$ – and solve iteratively Eq. (1):

1. we start the iteration with the choice $R_0 = 1 \text{ AU}$, namely in the grid cell (40, 398);
2. we find v_0 by dividing the required jet velocity by the velocity in PLUTO units inside the grid cell;
3. we calculate R_0 with Eq. (1);
4. we calculate the physical position of the grid cell using this new R_0 ;
5. if $R(z)$ of the grid cell is larger than 10 AU (100 AU), we move to another grid cell 10% closer to the jet axis (equatorial plane); if $R(z)$ of the grid cell is smaller than 10 AU (100 AU), we move to another grid cell 10% further away;
6. we stop the iteration when the grid cell does not change anymore between two steps.

The same results, perhaps more intuitively, can be achieved using the following graphical picture. We assume that only grid cells along a cone with indices $(i, 10i)$ are important. Using Eq. (1) and the relation $i = 4R/R_0$, we have to search for the intersection point

$$f(i) \equiv v(i, 10i) = \frac{v_{jet}}{v_0} = 4 v_{jet} \sqrt{\frac{R_{jet}}{GM}} \frac{1}{\sqrt{i}} \equiv g(i). \quad (\text{A.1})$$

Figure A.1 shows $f(i)$ for all models and $g(i)$ for $v_{jet} = 600 \text{ km s}^{-1}$ ($v_{jet} = 100 \text{ km s}^{-1}$ for comparison with models SC3

and SC5) and $M = 0.5 M_{\odot}$. After an initial drop close to the origin, $f(i)$ converges to an almost constant normalized velocity for $i > 7$ (i.e. $R_0 < 5.7 \text{ AU}$ for $R_{jet} = 10 \text{ AU}$) in the models ADO, SC1a-c and SC5 and for $i > 20$ (i.e. $R_0 < 2 \text{ AU}$) in the others. Its value increases from the untruncated model ADO (100) monotonically with increasing degree of truncation (150 in SC1a up to 300 in SC1g). The models SC2 and SC4 have values close to that of model SC1a.

Reducing the required mass or increasing the required jet velocity shifts the function $g(i)$ upwards and thus increases i of the intersection point and decreases R_0 , until $g(i)$ does not intersect with $f(i)$ anymore inside the computational domain. For example, we could not find acceptable sets of normalizations for the runs $(\dots, 1000, 0.2)$ in models ADO, SC1a–b, SC2 and SC4; in the models SC1c–g, normalizations were found for all runs. However, most of these runs were later excluded due to our requirement of $R_0 < 30 \text{ AU}$.

In the inner truncation models SC3 and SC5, the final value of $f(i)$ is much lower, only about 15, therefore both functions only intersect for small velocities. Again, most of the runs found were later excluded due to our requirement of $R_0 < 30 \text{ AU}$.

Appendix B: Reasons for the artefact of limb-brightening

If the number density is below the critical density, the emissivity of e.g. the [SII] $\lambda 6731$ line can be written as

$$\epsilon(T) = n_e n_{\text{SII}} f(T) = n_e n_S g(T) f(T), \quad (\text{B.1})$$

with n_e and n_{SII} the electron and ion density, respectively. The latter is a function of the total sulfur density n_S and the ionization fraction $g(T) = n_{\text{SII}}/n_S$. $f(T)$ usually has the form

$$f(T) = T^{-C} \exp(-D/T) \quad (\text{B.2})$$

with a powerlaw and an exponential cut-off. One can show that $\epsilon(T)$ has a maximum at temperatures of about $4 \times 10^4 \text{ K}$. For lower temperatures, $f(T)$ decreases steeply. For temperatures higher than about $6 \times 10^4 \text{ K}$, $g(T)$ decreases steeply. The latter cut-off is due to the assumption of ionization equilibrium used in OpenSESAME for calculating the level population and chemical composition, while the former is due to the exponential temperature dependence in Eq. (B.2), intrinsic to collisional excitation of a level of upper energy D . In Eq. (B.1), n_e is also a very steep function of T in ionization equilibrium.

Thus the main emission comes only from a thin shell of the jet, in which the temperature is exactly in the range of $(4-6) \times 10^4 \text{ K}$. By changing the temperature normalization, we can move the emitting shell on the axis, but the resulting jet widths are of the order of the *FWHM* of the Gaussian PSF. Therefore we have to have a constant temperature profile towards the axis.

Appendix C: Emission maps of the [OI] $\lambda 6300$ line for all models and runs

Here we present the emission maps of the [OI] $\lambda 6300$ line for all models and runs (500, \dots , \dots) for the sake of completeness.

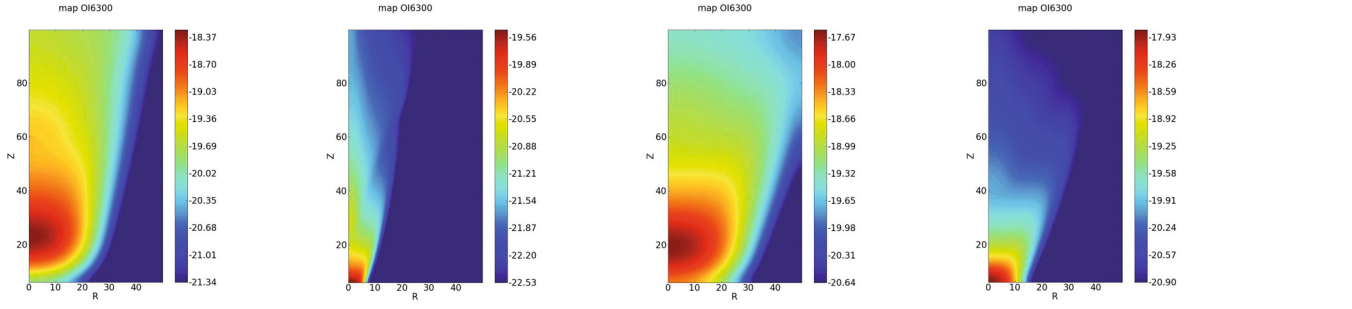


Fig. C.1. Synthetic emission maps of the [OI] $\lambda 6300$ line, convolved with a Gaussian PSF with a $FWHM$ of 15 AU, for model ADO and runs (500, 600, 0.2), (500, 600, 0.5), (500, 1000, 0.5), (500, 1000, 0.8).

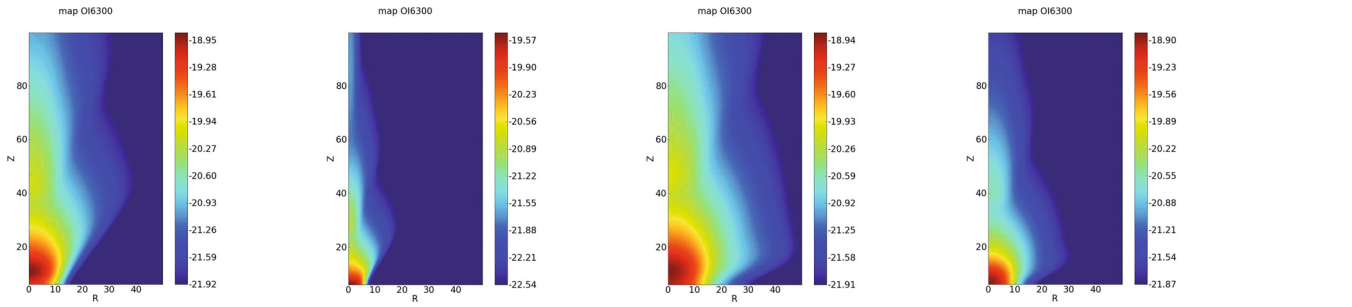


Fig. C.2. Synthetic emission maps of the [OI] $\lambda 6300$ line, convolved with a Gaussian PSF with a $FWHM$ of 15 AU, for model SC1a and runs (500, 600, 0.2), (500, 600, 0.5), (500, 1000, 0.5), (500, 1000, 0.8).

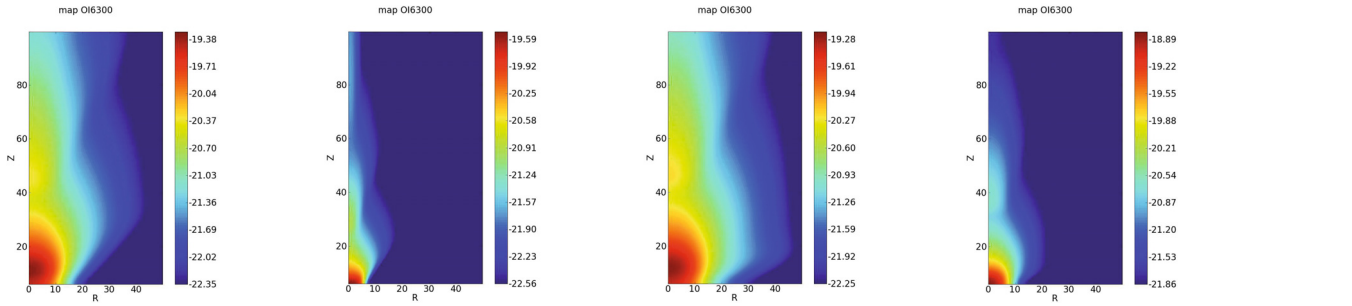


Fig. C.3. Synthetic emission maps of the [OI] $\lambda 6300$ line, convolved with a Gaussian PSF with a $FWHM$ of 15 AU, for model SC1b and runs (500, 600, 0.2), (500, 600, 0.5), (500, 1000, 0.5), (500, 1000, 0.8).

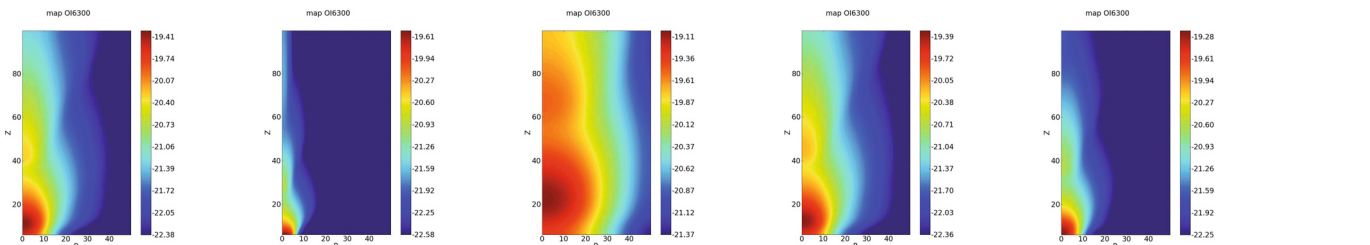


Fig. C.4. Synthetic emission maps of the [OI] $\lambda 6300$ line, convolved with a Gaussian PSF with a $FWHM$ of 15 AU, for model SC1c and runs (500, 600, 0.2), (500, 600, 0.5), (500, 1000, 0.2), (500, 1000, 0.5), (500, 1000, 0.8).

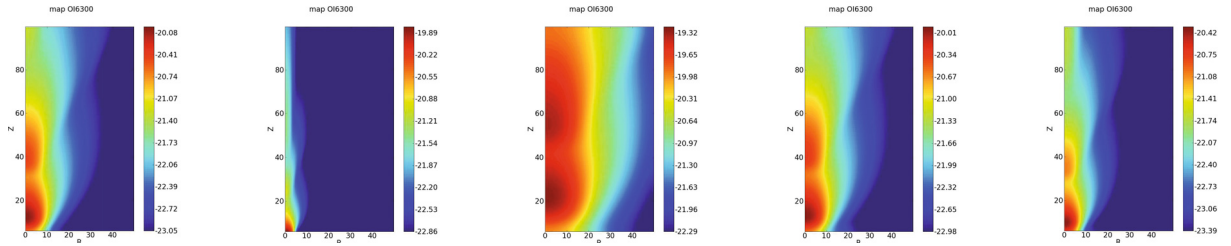


Fig. C.5. Synthetic emission maps of the [OI] $\lambda 6300$ line, convolved with a Gaussian PSF with a *FWHM* of 15 AU, for model SC1d and runs (500, 600, 0.2), (500, 600, 0.5), (500, 1000, 0.2), (500, 1000, 0.5), (500, 1000, 0.8).

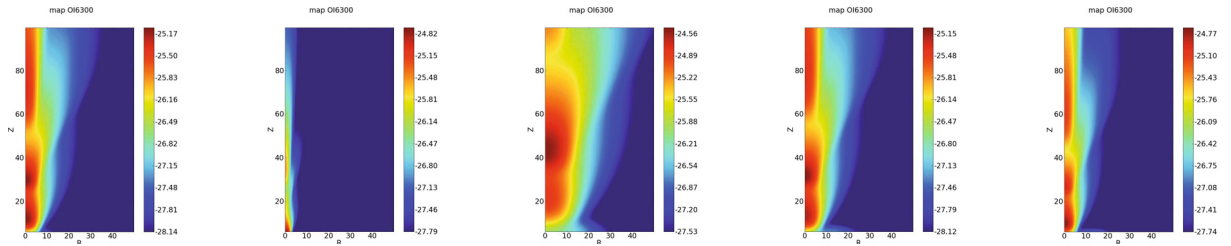


Fig. C.6. Synthetic emission maps of the [OI] $\lambda 6300$ line, convolved with a Gaussian PSF with a *FWHM* of 15 AU, for model SC1e and runs (500, 600, 0.2), (500, 600, 0.5), (500, 1000, 0.2), (500, 1000, 0.5), (500, 1000, 0.8).

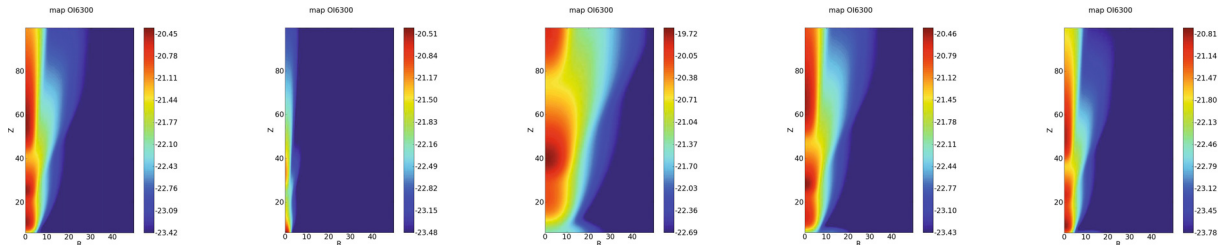


Fig. C.7. Synthetic emission maps of the [OI] $\lambda 6300$ line, convolved with a Gaussian PSF with a *FWHM* of 15 AU, for model SC1f and runs (500, 600, 0.2), (500, 600, 0.5), (500, 1000, 0.2), (500, 1000, 0.5), (500, 1000, 0.8).

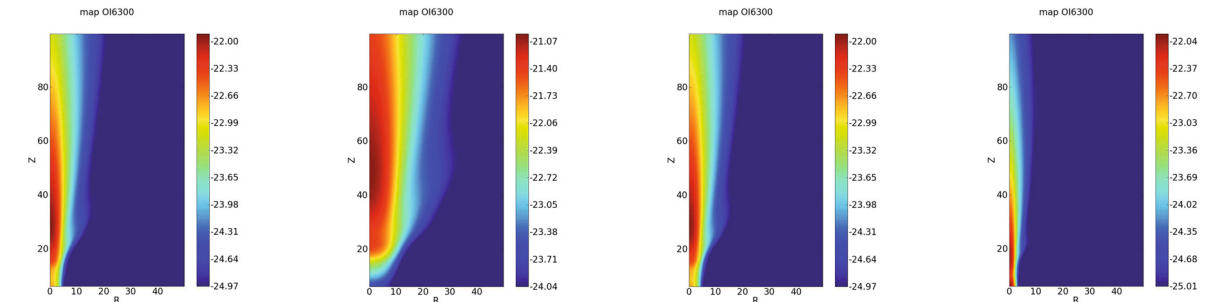


Fig. C.8. Synthetic emission maps of the [OI] $\lambda 6300$ line, convolved with a Gaussian PSF with a *FWHM* of 15 AU, for model SC1g and runs (500, 600, 0.2), (500, 1000, 0.2), (500, 1000, 0.5), (500, 1000, 0.8).

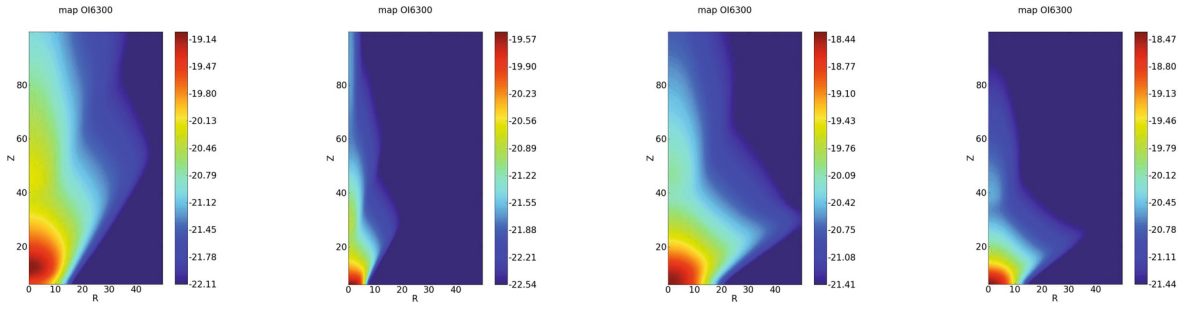


Fig. C.9. Synthetic emission maps of the [OI] $\lambda 6300$ line, convolved with a Gaussian PSF with a *FWHM* of 15 AU, for model SC2 and runs (500, 600, 0.2), (500, 600, 0.5), (500, 1000, 0.5), (500, 1000, 0.8).

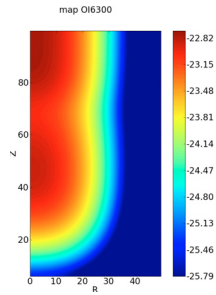


Fig. C.10. Synthetic emission maps of the [OI] $\lambda 6300$ line, convolved with a Gaussian PSF with a *FWHM* of 15 AU, for model SC3 and run (500, 100, 0.2).

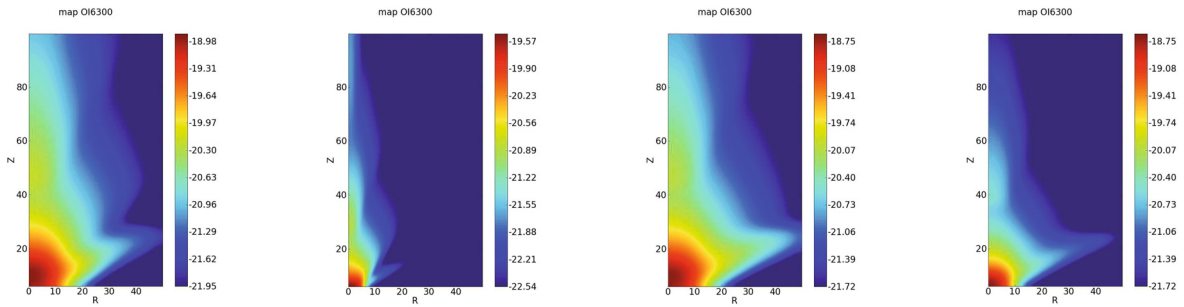


Fig. C.11. Synthetic emission maps of the [OI] $\lambda 6300$ line, convolved with a Gaussian PSF with a *FWHM* of 15 AU, for model SC4 and runs (500, 600, 0.2), (500, 600, 0.5), (500, 1000, 0.5), (500, 1000, 0.8).